RSC Advances

PAPER

View Article Online
View Journal | View Issue

Cite this: *RSC Adv.*, 2018, **8**, 11633

Fatigue endurance enhancement of Sn-doped $Pb(Lu_{1/2}Nb_{1/2})O_3$–$PbTiO_3$ ceramics

Chenxi Wang,[ab] Chao He,*[a] Zujian Wang,[a] Xiuzhi Li,[a] Xiaoming Yang,[a] Ying Liu[a] and Xifa Long*[a]

Received 24th January 2018
Accepted 19th March 2018

DOI: 10.1039/c8ra00732b

rsc.li/rsc-advances

Several mechanisms and methods have been proposed to study the nature of electric fatigue in ferroelectric materials with perovskite structure, including defect agglomeration, field screening and the reorientation of defect dipoles. To ascertain the effect of defect, defect dipoles in particular on the fatigue behavior in perovskite ferroelectrics, $0.51Pb(Lu_{1/2}Nb_{1/2})O_3$–$0.49PbTi_{1-x}Sn_xO_3$ ferroelectric ceramics were fabricated in this work. It is found that the fatigue endurance has been enhanced after Sn-doping. An abnormal strong self-rejuvenation of polarization was also detected for un-poled and un-aged samples resulting from the reorientation of defect dipoles. The defect dipoles were determined by the confirmed change of the valence of Sn ions and the appearance of oxygen vacancies. The reorientation was also confirmed by the internal bias of *P*–*E* hysteresis loops during the fatigue process. With more Sn doped into the matrix, the symmetry changed from a coexistence of rhombohedral and tetragonal phase to a rhombohedral phase. The remnant polarization decreased, while the coercive field first decreased then increased as *x* increased, which resulted from the composition variance and the effect of defect dipoles. It indicates that the defect dipoles play an important role in the electric fatigue behavior of Sn-doping PLN–PT ceramics.

1. Introduction

Ferroelectrics with perovskite structure have been the cornerstone of modern high-tech electrical devices such as actuators, piezoelectric transducers and acoustic transducers.[1–3] Among various ferroelectrics with a complex perovskite structure, $Pb(Lu_{1/2}Nb_{1/2})O_3$–$PbTiO_3$ (PLN–PT) solid solutions were found in which the morphotropic phase boundary (MPB) between tetragonal and rhombohedral phase is in the range of 0.49–0.51PT, exhibiting excellent electrical properties and high Curie temperature (T_C),[4–6] which makes the PLN–PT system a promising candidate for high-power transducer applications with a wide range of application temperature. In actual applications, devices are subjected to repetitive electric cycles. The severe degradation of reversible polarization and subsequent degradation of various electric properties will be caused by cyclic electric field, *i.e.* electric fatigue. Electric fatigue hinders the reliability and life length of ferroelectric devices severely.[7] Hence, a good electric fatigue endurance is highly desired for ferroelectric devices.[8]

Many researchers have studied the fatigue behavior of Pb-based ferroelectrics in recent years.[9–13] Many mechanisms and methods have been proposed to study the nature of electric fatigue: defect agglomeration,[14] field screening resulting from surface damage,[15] local phase decomposition[16] and so on. Most of these mechanisms are based on these two steps: first, cyclic electric field induces a creation of imperfections or a redistribution of intrinsic imperfections; second, the subsequent imperfections affect the reversible polarization.[17] Among all of the imperfections, point defects play an essential part because they affect the electric fatigue behavior significantly.[18,19] The existence of point defects in materials also affects almost every physical property of the matrix. Almost all of the unsolved problems of ferroelectrics have some relations with defects, including aging,[20] imprint[21,22] and the unwanted increment of leakage current.[23] It's of great significance to study the effect of point defects on ferroelectric materials. The most effective way to induce point defects is doping. Two kinds of point defects would be generated through doping: cation vacancies are generated *via* donor doping, and oxygen vacancies are generated through acceptor doping.[24] Whether cation vacancies and oxygen vacancies play positive or negative roles in the fatigue behavior of bulk ferroelectrics is still unclear. Chen *et al.* reported that fatigue endurance improved more for donor-doped $BaTiO_3$ ceramics than that of acceptor-doped materials.[25] However, better fatigue endurance has been reported for acceptor-doped $PbZrO_3$ ceramics than donor-doped $PbZrO_3$ ceramics.[26] Compared with the fatigue behavior of donor-doped ferroelectrics, it's more complicated in acceptor-doped

[a]*Key Laboratory of Optoelectronic Materials Chemistry and Physics, Fujian Institute of Research on the Structure of Matter, Chinese Academy of Sciences, Fuzhou 350002, Fujian, China. E-mail: hechao@fjirsm.ac.cn; lxf@fjirsm.ac.cn*
[b]*University of Chinese Academy of Sciences, Beijing, China*

ferroelectrics due to the high mobility of oxygen vacancies[27–30] and the defect dipoles formed between defect ions and oxygen vacancies.[31] The domain wall pinning due to the agglomeration of oxygen vacancies during the fatigue process hampers the motion of domain walls, leading to the detriment of fatigue endurance. While the defect dipoles formed in the bulk should reorient under strong bipolar electric field during the fatigue process, which results in more complicated fatigue behavior. Apart from the enhancement of fatigue endurance of acceptor-doped ferroelectrics mentioned above, some authors have found abnormal self-rejuvenation behavior of the remnant polarization (P_r) during the fatigue process for poled and fully aged Pb-based ferroelectric ceramics under cyclic bipolar electric field due to the de-pinning or de-aging effect of oxygen vacancies.[32,33] To our knowledge, this abnormal self-rejuvenation has not been found in un-poled and un-aged Pb-based ferroelectrics with perovskite structure, which has actually been found in this work. If well understood, the mechanism behind this phenomenon is bound to make great contribution to the materials science.

In this work, we focus on fatigue endurance enhancement of PLN–PT ceramics and study the effect of defect dipoles on electric fatigue behavior of acceptor-doped PLN–PT ceramics. 0.51PLN–0.49PT ceramic in the MPB region close to the rhombohedral side was chosen as the matrix in this work due to the excellent electric properties of this composition. It was found in the current work that for the composition 0.51PLN–0.49PT, the P_r decreases to half of the value measured at the beginning of the fatigue process before the number of cycles (n) increases up to 1.6×10^4. This fatigue endurance is very weak compared with PMNT ceramics, the P_r of which keeps nearly stationary even up to 10^4 cycles.[10] Hence it is very necessary to enhance the fatigue endurance of 0.51PLN–0.49PT ceramics to make them more reliable. In this work, SnO_2 was chosen as the dopant to obtain acceptor-doped 0.51PLN–0.49PT ceramics because there were many good works about Sn-doping in ferroelectrics like $BaTiO_3$,[34] $Pb(Ti_{0.65}Zr_{0.35})O_3$ (ref. 35) and $BaNbO_3$.[36] Sn was found to exist in oxides as both Sn^{2+} and Sn^{4+}.[37–39] We substituted Sn^{4+} ions for B-site Ti^{4+} ions. The valence change of Sn^{4+} thus led to the formation of oxygen vacancies to balance the charge misfit. To avoid the domain wall pinning of oxygen vacancies caused by aging effect, fatigue behavior was measured right after the annealing treatment. Ferroelectric, fatigue and dielectric characteristics of the samples with different Sn doping levels were studied, together with the chemical valence state of Sn and oxygen vacancies.

2. Experimental procedure

Sn ions modified PLN–PT ceramics with the formula of $0.51Pb(Lu_{1/2}Nb_{1/2})O_3$–$0.49PbTi_{1-x}Sn_xO_3$ ($x = 0$–0.2) were fabricated by the traditional solid-state reaction method using high purity (99.9%) PbO, Lu_2O_3, Nb_2O_5, TiO_2, SnO_2 as raw materials. Excess of 2 mol% of the total amount of PbO which was weighed according to the stoichiometry was added to compensate the evaporation of PbO during sintering. At first, all the raw materials were blended and ball-milled in ethanol with 2 mol% excess of PbO for 24 hours. Then the adequately milled powder was pressed into discs at 15 MPa and calcined at 850 °C in air for 3 hours. After calcination, the discs were remilled for 2 hours with 2 wt% polyvinyl alcohol (PVA) as a binder. Again, the powder was pressed into small pellets at 13 MPa, and the discs were heated up to 500 °C for 2 hours to eliminate PVA. At last, the discs were sintered at 930 °C to 970 °C for 3 hours in an Al_2O_3 crucible filled with $PbZrO_3$ which prevents the excessive evaporation of PbO.

The crystalline phase of sintered specimens was analyzed by X-ray diffractometer (XRD) (Miniflex 600, Rikagu, Japan) from 5° to 80° (2θ) with a speed of 2 deg min^{-1} and a step of 0.02 (2θ) at room temperature. Theoretical density of the ceramics was calculated through the XRD profile using the software Jade 6.0. The observations of the microstructure of the fractured surfaces of the specimens were carried out by a field emission scanning electron microscope (SEM, Hitachi SU-8010, Japan). The sintered disc ceramics were cut into rectangle with the area about 8 mm^2 to avoid edge effects, and polished to about 300 μm in thickness with 800 grit SiC papers, and then annealed at 500 °C for 3 hours to eliminate the aging effect. Right after the annealing, the samples were pasted with silver paste and then electrical measurements were made immediately. Ferroelectric characterizations and fatigue behavior were measured by the aixACCT TF Analyzer 2000 standard ferroelectric test system. Before the fatigue treatment, the polarization–electric field (P–E) hysteresis loops were measured under an AC field of 5 Hz with the amplitude of 60 kV cm^{-1}. It should be noted that the amplitude of the applied field was enhanced slowly in order not to break the sample. Then the samples were fatigued immediately. For fatigue behavior, the samples were subjected to a bipolar AC field with the amplitude of about 2 times of the coercive field (E_C) (determined before the fatigue treatment) and frequency of 100 Hz up to 3×10^6 cycles. Dielectric properties measurements were performed by Alpha-A high resolution impedance analyzer (Novocontrol GmbH). Oxygen vacancies and the oxidation states of Sn ions were investigated by X-ray photoelectron spectroscopy (XPS, ESCALAB 250Xi). The samples for XPS investigation were all polished to eliminate the influence of the surface state.

3. Results and discussion

3.1 Structure analysis

The XRD patterns of $0.51Pb(Lu_{1/2}Nb_{1/2})O_3$–$0.49PbTi_{1-x}Sn_xO_3$ ceramics with compositions of $x = 0$–0.2 at room temperature are presented in Fig. 1(a), showing perovskite structures with $x = 0$–0.12 and small amount of secondary phase compositions with $x > 0.14$ (the XRD profiles of which were enclosed by two dashed squares in the inset of Fig. 1(a)), which was found to be $Sn_2Nb_2O_7$ and cannot be eliminated easily by changing synthesis conditions. The pyrochlore phase was caused by the formation of Sn^{2+}. The appearance of Sn^{2+} made it easy to form the $Sn_2Nb_2O_7$ pyrochlore phase with Nb^{5+} ions. The valence state of Sn will be discussed later in the current article. In order to study the effect of Sn ions on the structure of PLN–PT ceramics, attention was paid to the XRD profiles of $(200)_C$

around $2\theta = 45°$. Shown in Fig. 1(b) were the profiles of (200) peaks of the composition of $x = 0$ and $x = 0.1$. For the pure PLN–PT ($x = 0$) ceramics, the (200) peak around $2\theta = 45°$ showed an asymmetrical peak, composed of three peaks with Gauss distribution. The ratio of the intensities of peak 1 and peak 3 is about 1 : 2. It is known that the profile of R(200) peak of rhombohedral (R) structure exhibits only a single sharp symmetrical peak because for rhombohedral phase, the relation among the lattice parameters is $a = b = c$, making the patterns of (200) and (002) peaks indistinguishable. While for the tetragonal (T) symmetry, the (200) peak ought to split into two peaks, corresponding to T(200)/(020) and T(002) with the ratio of the intensities of the two peaks about 2 : 1 because of $a = b \neq c$.[40,41] Obviously, peak 2 corresponds to the rhombohedral phase. Peak 1 and 3 correspond to the tetragonal phase. The $(200)_C$ (subscript C represents cubic) peak of all the doped compositions is sharper and more symmetrical than that of the virgin composition. Shown in Fig. 1(c) were the profile of (111) peak from $x = 0.02$ to $x = 0.12$. It could be seen that all the peaks showed asymmetric profile, which is a characteristic of rhombohedral structure.[42] So the dopant of Sn changed the symmetry from an MPB region to a rhombohedral phase, eliminating the tetragonal phase.

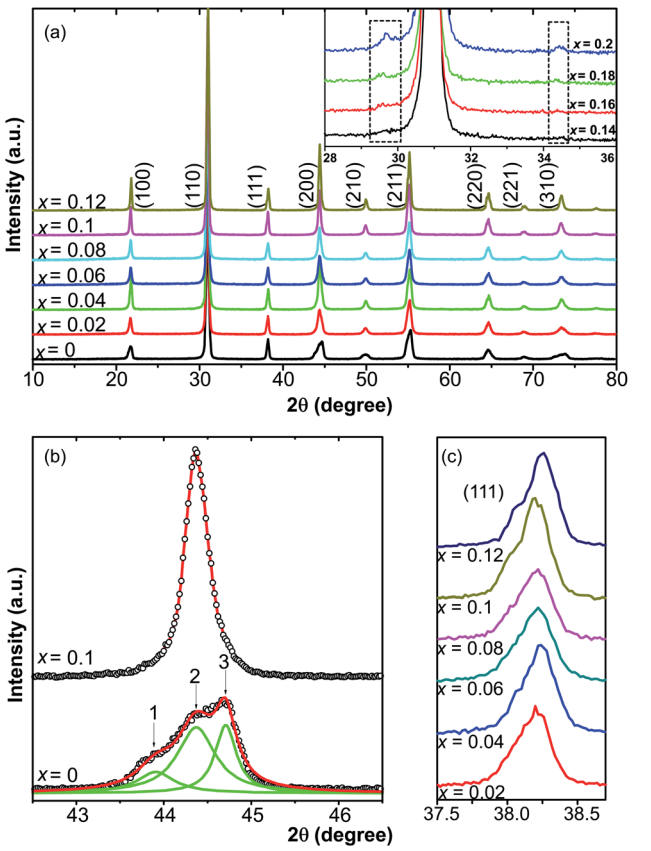

Fig. 1 (a) XRD patterns of $0.51Pb(Lu_{1/2}Nb_{1/2})O_3–0.49PbTi_{1-x}Sn_xO_3$ ceramics with $x = 0–0.12$. The inset shows the details between 28 and 36 degree, indicating a secondary phase. (b) $(200)_C$ profile of $x = 0$ and $x = 0.1$, showing that the dopant of Sn changed the symmetry from an MPB region to a pure rhombohedral phase, erasing the tetragonal phase. (c) The profile of (111) peak with $x = 0.02–0.12$.

The SEM micrographs of the selected ceramics ($x = 0$, 0.04, 0.08) are shown in Fig. 2, showing highly dense structure with clear grain boundaries, indicating intergranular structure. Theoretical density of the refined XRD data was calculated and the relative density of each sample without secondary phase is more than 90% of the theoretical density, namely, the low level of porosity. The average size of grains for the virgin specimens is about 7–9 μm. The grains shrink slightly with the increase of x

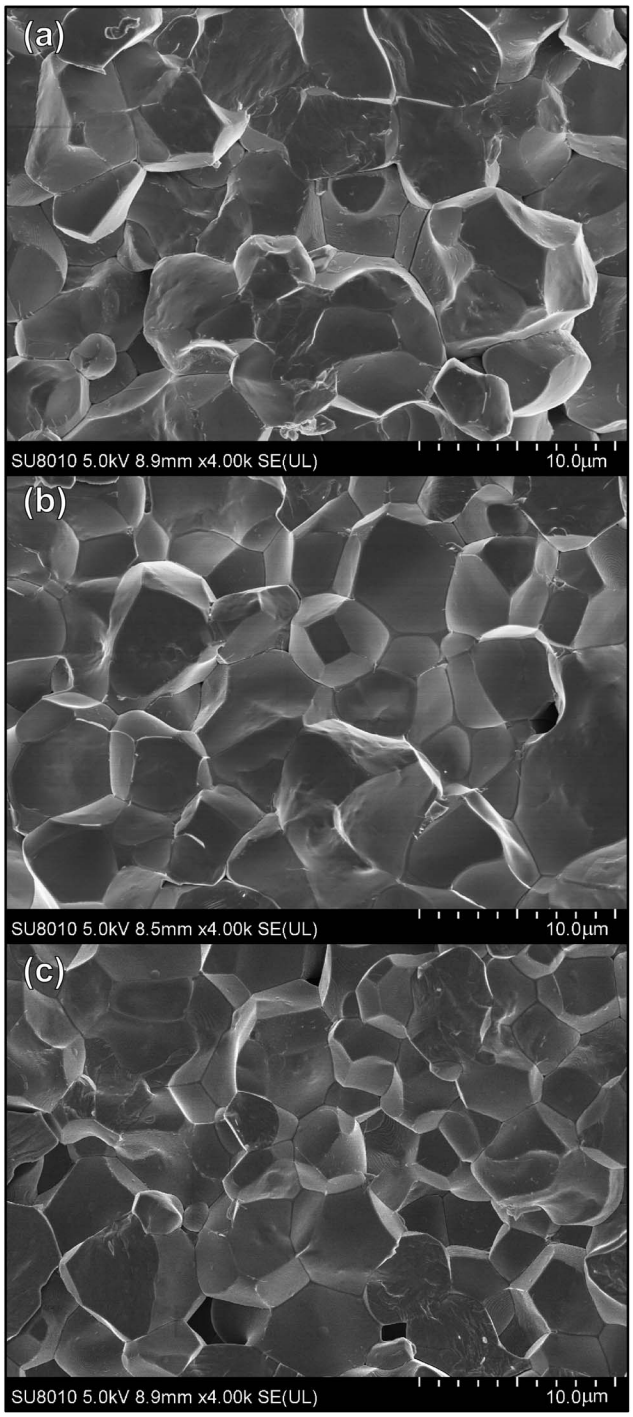

Fig. 2 SEM micrographs of fractured surfaces of $0.51Pb(Lu_{1/2}Nb_{1/2})O_3–0.49PbTi_{1-x}Sn_xO_3$ ceramics: (a) $x = 0$; (b) $x = 0.04$; (c) $x = 0.08$.

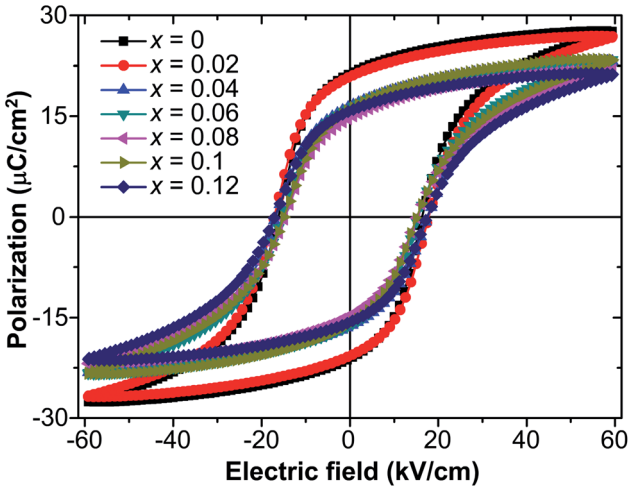

Fig. 3 *P–E* hysteresis loops of $0.51Pb(Lu_{1/2}Nb_{1/2})O_3–0.49PbTi_{1-x}Sn_xO_3$ ceramics.

Table 1 Ferroelectric properties of $0.51Pb(Lu_{1/2}Nb_{1/2})O_3–0.49PbTi_{1-x}Sn_xO_3$ ceramics

x	P_r ($\mu C\ cm^{-2}$)	P_{sat} ($\mu C\ cm^{-2}$)	$P_{1.1E_C}$ ($\mu C\ cm^{-2}$)	E_C ($kV\ cm^{-1}$)	R_{sq}
0	21.2	27.6	25.0	16.2	1.95
0.02	20.7	26.8	24.6	17.5	1.96
0.04	16.3	23.2	20.4	17.3	1.95
0.06	16.1	24.0	20.1	15.4	1.92
0.08	14.6	22.8	18.6	14.9	1.91
0.1	15.9	23.8	20.2	15.0	1.94
0.12	15.7	21.7	19.1	17.3	1.94

with about 4–5 μm for $x = 0.08$. So the substitution of Sn for Ti ions has significant influence on the morphology of PLN–PT ceramics.

3.2 Ferroelectric properties

Fig. 3 presents the *P–E* hysteresis loops of the selected Sn-doped and un-doped PLN–PT ceramics. Well-saturated loops were found for every sample, indicating good ferroelectricity. The squareness (R_{sq}) of the loops quantifies the ferroelectricity from one aspect, and could be calculated *via* the following equation:[43]

$$R_{sq} = \frac{P_r}{P_{sat}} + \frac{P_{1.1E_C}}{p_r}, \quad (1)$$

where P_r is the remnant polarization, defined as $|p_r^+ - p_r^-|/2$ in the current work. p_r^+ and p_r^- are the positive and negative value of P_r, respectively. P_{sat} is the saturation polarization. $P_{1.1E_C}$ is the polarization at the electric field 1.1 times of E_C, defined as $|E_C^+ - E_C^-|/2$ in the current work. E_C^+ and E_C^- are the positive and negative values of E_C, respectively. The values of P_r, P_{sat}, $P_{1.1E_C}$, E_C and R_{sq} for every selected sample were listed in Table 1. For a perfect loop, $R_{sq} = 2$. It can be seen that R_{sq} for the studied samples in this work are all larger than 1.91 and show little fluctuation with the variance of x, showing good squareness of the loops.

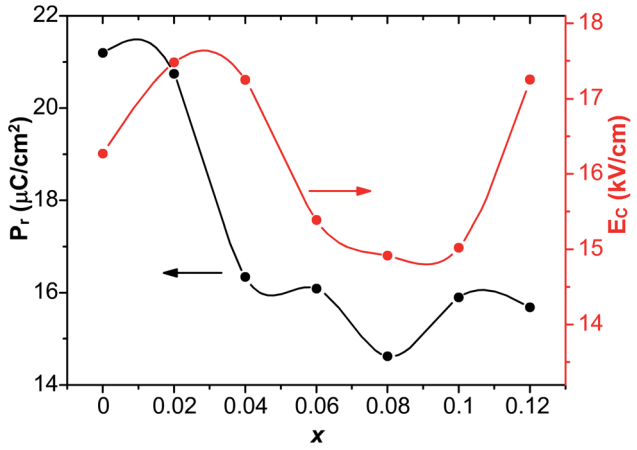

Fig. 4 The values of P_r and E_C of $0.51Pb(Lu_{1/2}Nb_{1/2})O_3–0.49PbTi_{1-x}Sn_xO_3$ ceramics with respect to the content of Sn.

To investigate the relation between the content of Sn and ferroelectric properties, the variation of P_r and coercive field E_C in terms of the content of Sn is depicted in Fig. 4. P_r drops from $x = 0$ to $x = 0.04$, then changes little with x increasing. E_C drops to the minimum at $x = 0.08$, then magnifies with more the

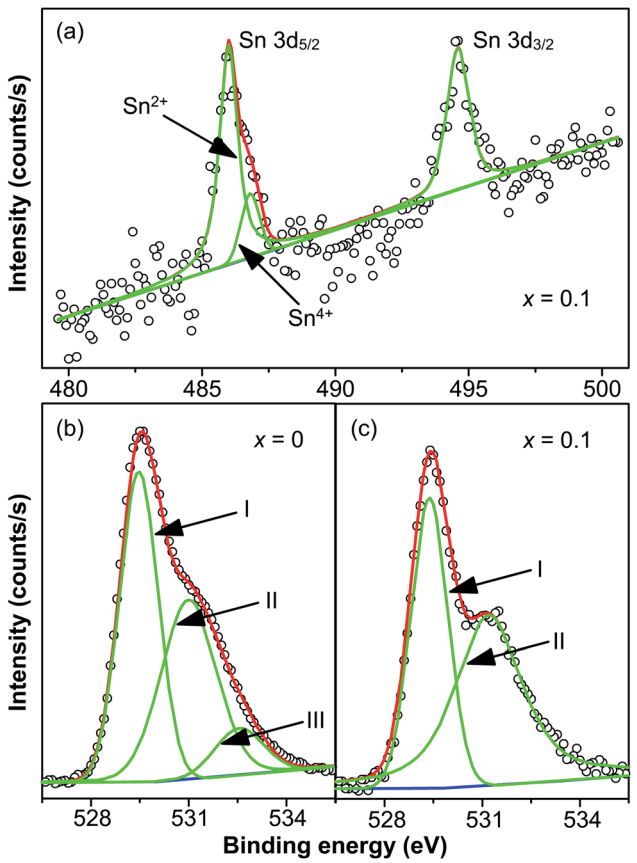

Fig. 5 (a) XPS spectrum of Sn 3d core level of $x = 0.1$ at room temperature, and XPS spectrum of O 1s core level of (b) $x = 0$ and (c) $x = 0.1$ at room temperature. Circles were the measured spectra, red curves were the fitted curves and green curves were the individual Gaussian peaks and blue lines are the Tougaard-type background.

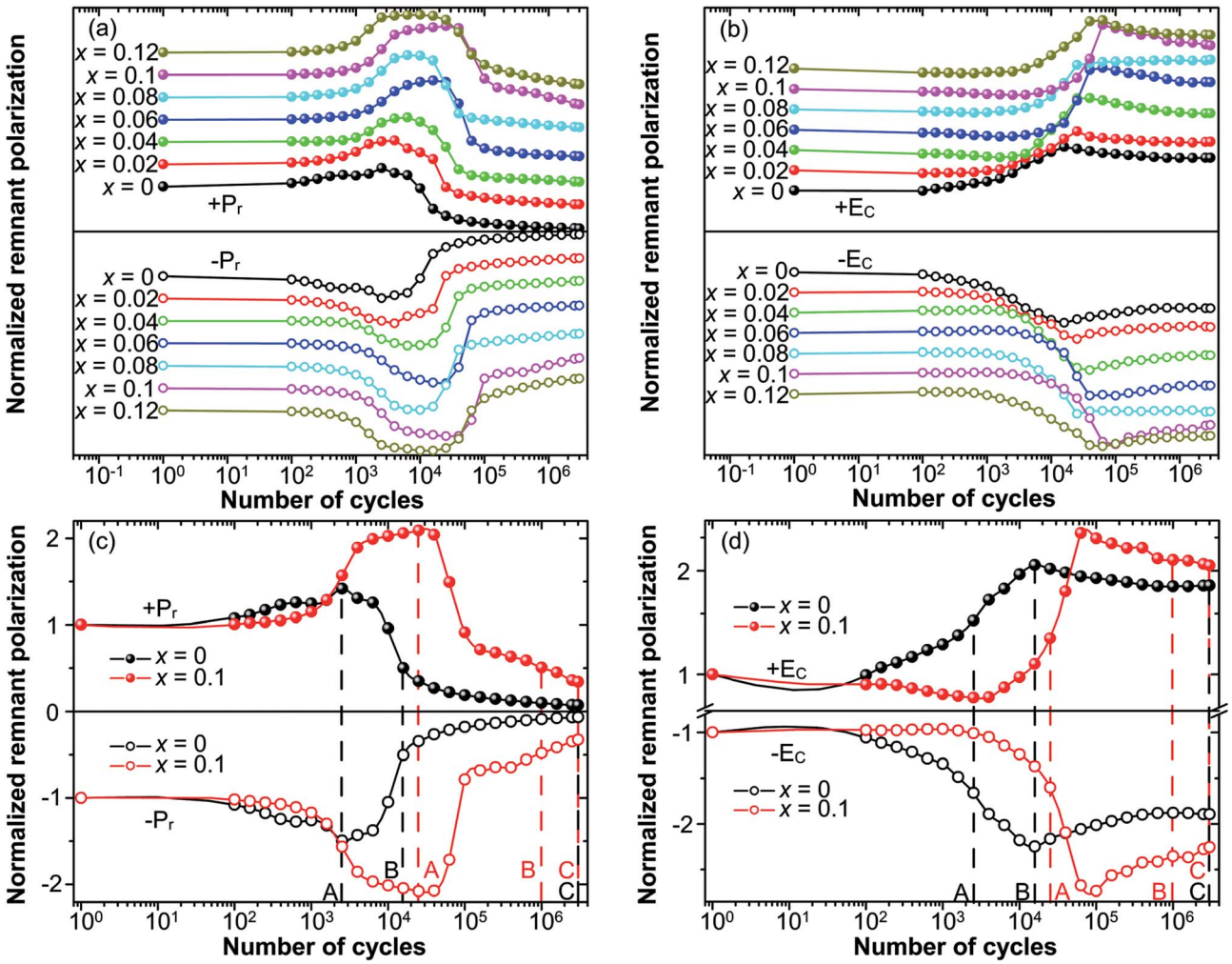

Fig. 6 Plots of (a) normalized $\pm P_r$ and (b) normalized $\pm E_C$ as a function of the number of cycles for $0.51Pb(Lu_{1/2}Nb_{1/2})O_3$–$0.49PbTi_{1-x}Sn_xO_3$ ceramics under an applied bipolar field of $2E_C$ for each composition at 100 Hz. Normalized P_r and normalized E_C of the composition $x = 0$ and $x = 0.1$ were extracted and shown in (c) and (d) respectively.

content of Sn. The decrement of P_r and E_C at low-Sn-ion region is attributed to the decrease of the content of $PbTiO_3$ (PT). The magnifying of E_C at $x > 0.08$ mainly results from the effect of defect dipoles formed as $Sn''_{Ti} - V_O^{\cdot\cdot}$. It is found that when calcined at high temperature, the Sn^{4+} of SnO_2 partly reduces to Sn^{2+} to form a mix state of the valence of +4 and +2.[39] The multivalent behavior of Sn has already been investigated previously.[44,45] The evidence of the change of valence state of Sn ions in this work will be presented below. The change of valence state from +4 to +2 thus leads to the formation of oxygen vacancies to balance the charge misfit. As a result, defect

Table 2 Fatigue behavior of $0.51Pb(Lu_{1/2}Nb_{1/2})O_3$–$0.49PbTi_{1-x}Sn_xO_3$ ceramics at the point at which P_r began to decrease to half of P_r measured at $n = 1$

x	n (cycles)	% change of E_C
0	15 849	116.2
0.02	24 821	95.6
0.04	35 558	127.5
0.06	68 013	150.2
0.08	100 096	116.8
0.1	10^6	125.1
0.12	371 735	88.8

Table 3 Fatigue behavior of ferroelectric properties for $x = 0$ and $x = 0.1$ at different number of cycles[a]

x	n (cycles)	P_r ($\mu C\ cm^{-2}$)	E_C ($kV\ cm^{-1}$)	% change of P_r	% change of E_C	Note
0	2512	33.4	26.3	45.6	54.4	A
	15 849	11.6	36.8	−49.7	116.2	B
	3×10^6	1.6	31.6	−93.1	85.2	C
0.1	25 119	34.6	22.2	108.4	43.5	A
	10^6	8.2	34.8	−50.6	125.1	B
	3×10^6	5.5	33.4	−66.6	116.2	C

[a] A, P_r increases to its maximum; B, P_r decreases to below 50% of the value of $n = 1$; C, the end of the fatigue process.

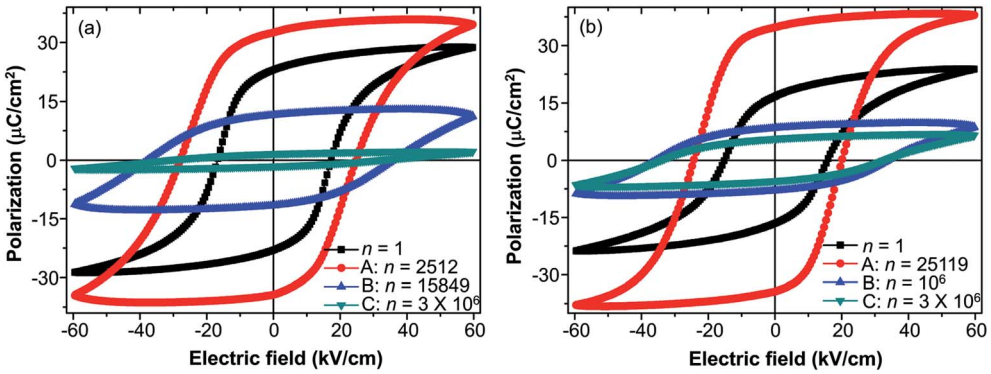

Fig. 7 P–E hysteresis loops of (a) $x = 0$ and (b) $x = 0.1$ at different points: A, at which P_r increases to its maximum; B, at which P_r decreases to below 50% of the value of $n = 1$; C, at the end of the fatigue process.

dipoles $Sn''_{Ti} - V_O^{\cdot\cdot}$ were formed. At $x < 0.1$, oxygen vacancies were not dense enough to have conspicuous effect on the materials, on which the decrease of the content of PT have more pronounced influence. At $x > 0.08$, enough oxygen vacancies were generated to form defect dipoles, leading the domain stability to be strengthened by the effect of defect dipoles. This effect stemmed from a symmetry-conforming property of point defects.[31] The irreversible defect dipoles make the switching of spontaneous polarization much harder, resulting in an increment of E_C at $x > 0.08$.

The chemical valence state of Sn and oxygen vacancies was examined X-ray photoelectron spectroscopy. Fig. 5(a) shows the XPS spectrum of Sn 3d core level of $x = 0.1$ at room temperature, showing two peaks in the binding energy range between 480 and 500 eV. The two peaks centered at 486.02 and 494.6 eV are for Sn $3d_{5/2}$ and Sn $3d_{3/2}$ respectively. Interestingly, two peaks centered at 486.02 and 486.84 eV are displayed after the fitting of the Sn $3d_{5/2}$ peak. It is reported that the two peaks of Sn $3d_{5/2}$ peak correspond to two valence states: Sn^{2+} (486.2 eV) and Sn^{4+} (487.1 eV).[39] Hence it is believed that both Sn^{2+} (486.02 eV) and Sn^{4+} (487.1 eV) exist in doped samples. The intensity of Sn^{2+} peak was much larger than the peak of Sn^{4+}, indicating that most Sn^{4+} ions were reduced to Sn^{2+} during the high-temperature calcination. This also supports the result discussed above that a pyrochlore phase with $Sn_2Nb_2O_7$, in which the valence of Sn ions is +2, is formed as a secondary phase at high-level dopant.

The reduction of the valence state of Sn ions leads to the formation of oxygen vacancies to compensate the misfit of charge, which is demonstrated by the XPS of O 1s core level of $x = 0$ and $x = 0.1$ shown in Fig. 5(b) and (c). It should be noted that in Fig. 5, circles are the measured spectra, red curves are the fitted curves, green curves are the fitted Gaussian peaks and blue lines are the Tougaard-type background. The spectrum of $x = 0$ is well fitted with three Gaussian peaks with a Tougaard-type background, plotted as blue curves in the figures. The peaks are located at 529.46 eV (O_I), 531 eV (O_{II}) and 532.54 eV (O_{III}). The spectrum of $x = 0.1$ is well fitted with two Gaussian peaks with a Tougaard-type background. The centers of the peaks are centered at 529.38 eV (O_I) and 531.24 eV (O_{II}). Peak O_I is associated with oxygen ions incorporated in the lattice sites in materials with perovskite structure. Peak O_{II} is attributed to the formation of oxygen vacancies. Peak O_{III}, which was not found in the spectrum of $x = 0.1$, resulted from the chemisorbed oxygen or dissociated oxygen.[46] Similar cases were also reported in several works.[28,47–49] The ratio of the area of O_{II} and O_I (denoted as R_a) was also calculated to determine the density of oxygen vacancies. For $x = 0$, $R_a = 0.85$, while for $x = 0.1$, $R_a = 1.28$, suggesting that oxygen vacancies of $x = 0.1$ are denser than that of $x = 0$. Hence the reduction of valence state of Sn^{4+} ions leads to the formation of oxygen vacancies, and defect dipoles are formed.

3.3 Fatigue behavior

The fatigue behavior was studied as shown in Fig. 6. Fig. 6(a and b) show the variation of P_r and E_C of all of the compositions measured at different n. For comparison, P_r and E_C were normalized to the corresponding values measured at the first circle. It can be easily seen that the curves of P_r and E_C of the studied samples show the similar trends. For precise study, the

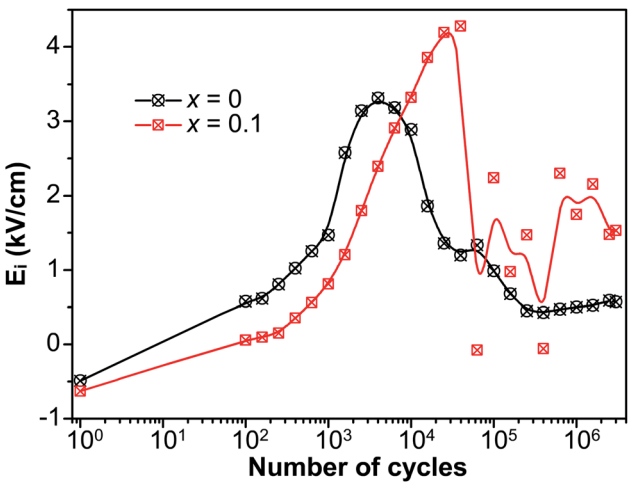

Fig. 8 The internal bias (E_i) of P–E hysteresis loops *versus* the number of cycles (n) during the fatigue process.

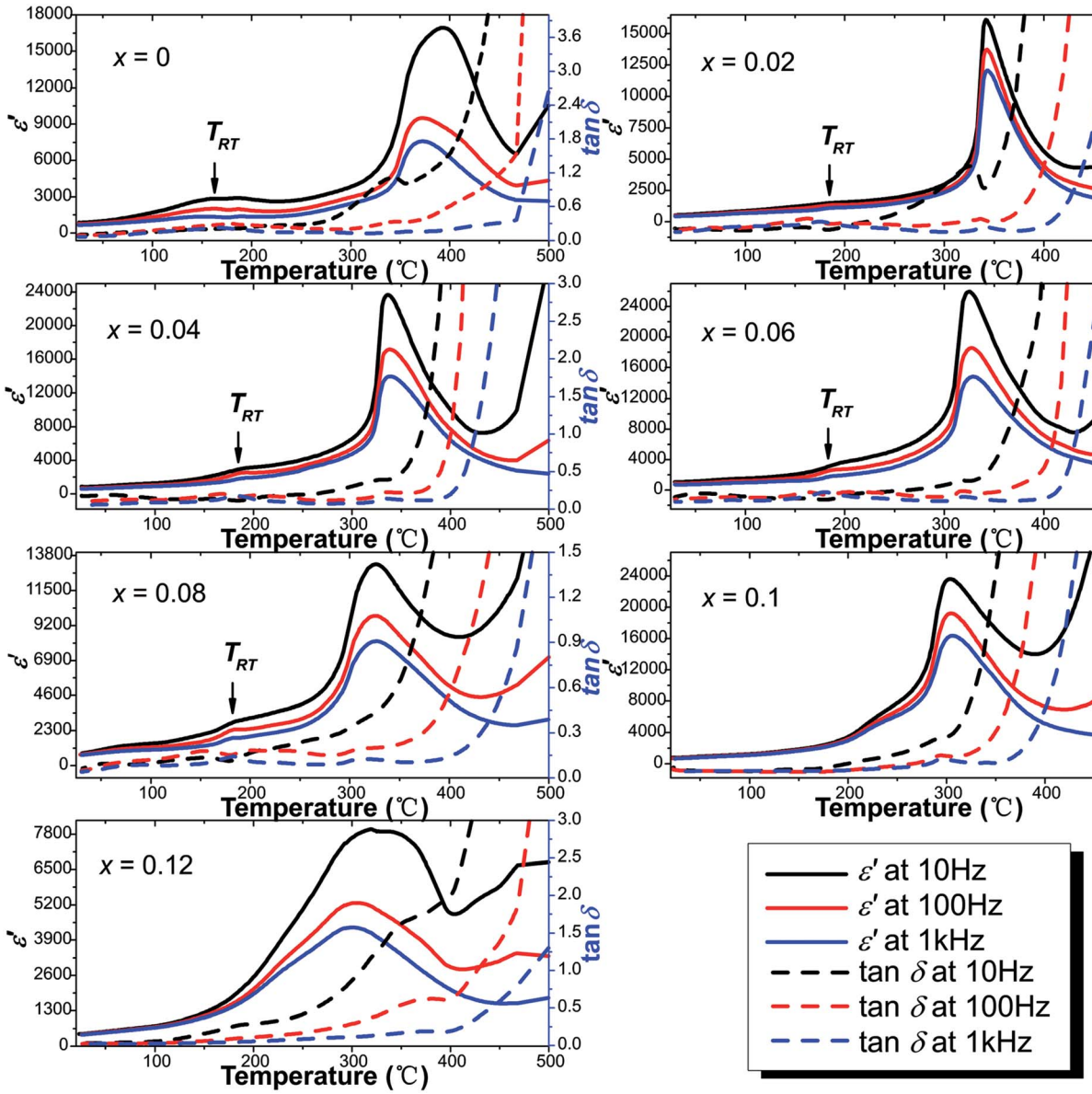

Fig. 9 Temperature dependence of the real part of dielectric constant and dielectric loss.

extracted curves of $x = 0$ and $x = 0.1$ compositions are shown in Fig. 6(c and d). P_r of both $x = 0$ and $x = 0.1$ shows an abnormal self-rejuvenation in the middle of the fatigue process, different from normal electric fatigue behavior of ferroelectrics, which doesn't show increment before decrement.[12,50–53] E_C of $x = 0$ first increased then decreased, with peak value located near point A. For $x = 0.1$, E_C experienced a decrement before increasing to the peak value, after which decreased. Generally, an increase of E_C was observed after the fatigue treatment for bulk ferroelectrics.[54] The abnormal behavior of E_C for $x = 0.1$ and P_r shall be discussed later.

The study of fatigue behavior of Sn-doped PLN–PT ceramics indicate that the fatigue endurance is enhanced greatly with Sn doped. In the following, we give some elucidation. Special attention was focused on: point A, at which P_r reaches maximum; point B, at which P_r decreases to half of the value of the first circle; and point C, at the end of the fatigue process, 3×10^6 cycles in the current work. To evaluate the fatigue endurance, the variation of the values of P_r and E_C at point B is listed in Table 2, indicating enhanced fatigue endurance of doped samples, because the value of P_r of all of the doped samples drops to half at more cycles than that of undoped samples. Compared with $x = 0$ ($n = 15\,849$), the cycles are $n = 10^6$ for $x = 0.1$, which is elevated by two orders of magnitude. The variation of the value of P_r and E_C of $x = 0$ and $x = 0.1$ compositions at point A, B, C are listed in Table 3. At point A, the value of P_r increases 45.6% for $x = 0$, while there is a 108.38% augment of P_r for $x = 0.1$. To have a direct understanding, the P–E hysteresis loops of $x = 0$ and $x = 0.1$ at three points and first cycle ($n = 1$) are presented in Fig. 7. At $n = 1$ for both compositions, the loops are not pinched or displaced, characteristic of the un-poled and un-aged case. For $x = 0$, the squareness increases from 1.96 to

1.97 from $n = 1$ to $n = 2512$, and the squareness shows an increment from 1.95 to 1.995 from $n = 1$ to $n = 25\,119$ for $x = 0.1$. The improvement of the squareness of $x = 0.1$ is greater than that of $x = 0$, apart from the more improvement of P_r value. It could also be seen that after 3×10^6-cycle fatigue treatment, the *P–E* hysteresis loop of $x = 0$ almost withers to a straight line clinging to the *x*-axis, while the loops of $x = 0.1$ still retained a moderate shape. This also helped elucidate the enhancement of fatigue endurance of the material *via* Sn doping.

As above mentioned, the abnormal behavior of P_r and E_C is attributed to the effect of the reorientation of defect dipoles. The abnormal increment has also been reported for acceptor doped PZT-based ceramics.[32,33] But the PZT samples studied before fatigue treatment were poled and fully aged. Such abnormal behavior, to our knowledge, has not been reported for un-poled and un-aged acceptor-doped ferroelectric materials with perovskite structure. It is known that oxygen vacancies have high mobility. Under strong electric field, charged defect dipoles can migrate even at a relatively low temperature.[55] Defect dipoles thus reorient and become more reversible under strong bipolar electric field. The reorientation and enhanced reversibility of defect dipoles under the bipolar field make the switching of spontaneous polarization much easier.[32] The release of spontaneous polarization from defect dipoles thus leads to the increase of P_r (for both $x = 0$ and $x = 0.1$) and decrease of E_C (for $x = 0.1$) at the first half part of the fatigue process. The fact mentioned above that P_r of $x = 0.1$ increases much more than that of $x = 0$ at point A suggests that more defect dipoles were generated and reoriented in the sample of $x = 0.1$, supporting the conclusion we drew above that the dopant of Sn ions leads to the formation of oxygen vacancies. The decrease of P_r and E_C after point A was the result of the field-shielding effect, resulting from the formation of layers with weak ferroelectric and dielectric properties under large number of cyclic electric field. And it is clear that in the fatigue process the reorientation of defect dipoles dominated before point A and field-shielding effect dominated after point A.

It is well known that there exists a correlation between the magnitude of internal bias field and the alignment of defect dipoles.[56] To further manifest the reorientation of defect dipoles, the internal bias with respect to *n* during the fatigue process is plotted in Fig. 8. The internal bias field in the current work is defined as $E_i = (E_- - E_+)/2$, where E_+ and E_- are the magnitude of the intersections of the *P–E* hysteresis loops and the electric field axis. E_i of both $x = 0$ and $x = 0.1$ increased to maximum near point A. The maximum of E_i for $x = 0.1$ appear at more cycles than that of $x = 0$, and the peak value of E_i of $x = 0.1$ is also larger than that of $x = 0$. It suggests that much more defect dipoles are formed and reorient in the sample of $x = 0.1$. In addition, a rather drastic fluctuation was detected of $x = 0.1$ after reaching the maximum. It is due to the competition between the reorientation of defect dipoles and the field-shielding effect, and it is this competition that leads to the enhancement of fatigue endurance of fatigue endurance.

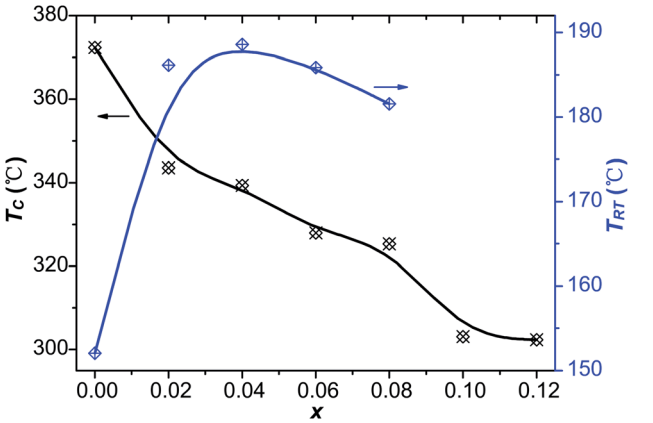

Fig. 10 The variation of T_{RT} and T_C in terms of *x*.

Table 4 Dielectric properties of $0.51Pb(Lu_{1/2}Nb_{1/2})O_3$–$0.49PbTi_{1-x}Sn_xO_3$ ceramics

x	ε' at RT	tan δ at RT	T_{RT} (°C)	T_C (°C)
0	869.2	0.09	152.0	372.3
0.02	524.4	0.07	186.2	343.5
0.04	844.8	0.17	188.6	339.4
0.06	1060	0.16	186.0	327.9
0.08	795.4	0.06	181.6	325.3
0.1	759.3	0.07	—	303.1
0.12	450.1	0.03	—	302.4

3.4 Dielectric properties

Fig. 9 shows the temperature dependence of the real part of the relative dielectric constant (ε') and the dielectric loss (tan δ) of the virgin and Sn-doped PLN–PT ceramics at the frequency of 10 Hz, 100 Hz and 1k Hz, respectively. Two peaks were detected in samples with $x \leq 0.08$. The sharper one corresponds to Curie temperature T_C, and the lesser one below T_C is known as rhombohedral–tetragonal transition temperature, denoted as T_{RT}. For samples with $x \geq 0.1$, T_{RT} disappears. The values of ε', tan δ, T_{RT} and T_C of the studied compositions were listed in Table 4. The variation of T_{RT} and T_C with respect to the content of Sn is shown in Fig. 10. It can be seen that T_C decreases from 372 °C to 302 °C as *x* increases. T_{RT} first increases, reaching maximum at $x = 0.04$, then decreases as *x* increases to 0.08, after which T_{RT} disappears. It is found that the trend of T_C and T_{RT} of this work fits well to that of PLN–PT crystals that Liu *et al.* reported,[4] in which T_C of PLN–PT also decrease as the content of PT decreases, and the T_{RT} also shows a small peak around the composition 0.55PLN–0.45PT.

4. Conclusions

In summary, the structure, electric fatigue behavior and related electric properties of $0.51Pb(Lu_{1/2}Nb_{1/2})O_3$–$0.49PbTi_{1-x}Sn_xO_3$ ceramics were studied. The valence state of Sn was examined by XPS to change from +4 to +2 during high-temperature calcination so that the oxygen vacancies were created to balance the charge misfit. At high level of Sn content, defect dipoles caused

by Sn ions and oxygen vacancies induce an increment of E_C. The electric fatigue endurance is enhanced after the doping of Sn. The best fatigue endurance is achieved at composition $x = 0.1$, n of which was elevated by two orders of magnitude. An abnormal strong self-rejuvenation of the P_r was also detected for un-poled and un-aged samples. The enhancement of fatigue endurance and abnormal self-rejuvenation result from the reorientation of defect dipoles $Sn''_{Ti} - V_O^{\cdot\cdot}$. The temperature dependence of the relative dielectric constant of different compositions shows that the T_C decreased as the content of Sn increased and the T_{RT} decreased after an increment at $x < 0.04$. In this work, we gave evidence that defect dipoles not only play a positive role in the electric fatigue behavior of un-poled and un-aged acceptor-doped ferroelectric materials with perovskite structure, but also induce an abnormal self-rejuvenation behavior during the fatigue process.

Conflicts of interest

There are no conflicts to declare.

Acknowledgements

This work was supported by National Natural Science Foundation of China (grant no. 11404331, 91422303, 11504373, 51602308), Youth Innovation Promotion Association CAS and "Chunmiao" Talents Program for Young Scientists of Haixi Institute, CAS (CMZX-2016-006).

References

1 S. Zhang and F. Li, *J. Appl. Phys.*, 2012, **111**, 031301.
2 X. F. Long, J. B. Lin, X. Z. Li, Z. J. Wang and Z.-G. Ye, *Cryst. Growth Des.*, 2009, **9**, 657–659.
3 A. A. Bokov and Z.-G. Ye, *J. Mater. Sci.*, 2006, **41**, 31–52.
4 Y. Liu, X. Z. Li, Z. J. Wang, C. He, T. Li, L. D. Ai, T. Chu, D. F. Pang and X. F. Long, *CrystEngComm*, 2013, **15**, 1643–1650.
5 D. Q. Shen, X. Z. Li, Z. J. Wang, Y. Liu, C. He, T. Li, H. Tailor and X. F. Long, *Mater. Lett.*, 2012, **84**, 1–4.
6 M. Antonova, L. Shebanovs, M. Livinsh, J. Y. Yamashita, A. Sternberg, I. Shorubalko and A. Spule, *J. Electroceram.*, 2000, **4**, 179–187.
7 V. V. Shvartsman, A. L. Kholkin, C. Verdier, Z. Yong and D. C. Lupascu, *J. Eur. Ceram. Soc.*, 2005, **25**, 2559–2561.
8 B. Rawal, N. N. Wathore, B. Praveenkumar and H. S. Panda, *J. Mater. Sci.: Mater. Electron.*, 2017, **28**, 16426–16432.
9 N. Balke, D. C. Lupascu, T. Granzow and J. Roedel, *J. Am. Ceram. Soc.*, 2007, **90**, 1081–1087.
10 M. Promsawat, N. Promsawat, S. Jiansirisomboon, O. Namsar, F. Marlton, J. Daniels and S. Pojprapai, *J. Eur. Ceram. Soc.*, 2017, **37**, 4609–4616.
11 A. A. Jeyaseelan, D. Rangappa and S. Dutta, *Thin Solid Films*, 2017, **642**, 136–141.
12 F.-J. Yang, X. Cheng and Y. Zhang, *Ceram. Int.*, 2016, **42**, 2324–2329.
13 N. M. Murari, S. Hong, H. N. Lee and R. S. Katiyar, *Appl. Phys. Lett.*, 2011, **99**, 052904.
14 J. Nuffer, D. C. Lupascu and J. Rodel, *Acta Mater.*, 2000, **48**, 3783–3794.
15 J. Glaum, T. Granzow, L. A. Schmitt, H.-J. Kleebe and J. Roedel, *Acta Mater.*, 2011, **59**, 6083–6092.
16 X. J. Lou, M. Zhang, S. A. T. Redfern and J. F. Scott, *Phys. Rev. B: Condens. Matter Mater. Phys.*, 2007, **75**, 224104.
17 A. K. Tagantsev, I. Stolichnov, E. L. Colla and N. Setter, *J. Appl. Phys.*, 2001, **90**, 1387–1402.
18 Q. Zhang and R. W. Whatmore, *Mater. Sci. Eng., B*, 2004, **109**, 136–140.
19 S. J. Kang and Y. H. Joung, *J. Mater. Sci.*, 2007, **42**, 7899–7905.
20 L. X. Zhang and X. Ren, *Phys. Rev. B: Condens. Matter Mater. Phys.*, 2005, **71**, 174108.
21 M. Dawber, K. M. Rabe and J. F. Scott, *Rev. Mod. Phys.*, 2005, **77**, 1083–1130.
22 C. A-Paz de Araujo, J. D. Cuchiaro, L. D. McMillan, M. C. Scott and J. F. Scott, *Nature*, 1995, **374**, 627–629.
23 D. Damjanovic, *Rep. Prog. Phys.*, 1998, **61**, 1267–1324.
24 P. Jaiban, A. Watcharapasorn, R. Yimnirun, R. Guo and A. S. Bhalla, *J. Alloys Compd.*, 2017, **695**, 1329–1335.
25 J. Chen, M. P. Harmer and D. M. Smyth, *J. Appl. Phys.*, 1994, **76**, 5394–5398.
26 S. Priya, H. W. Kim, J. Ryu and K. Uchino, *Appl. Phys. Lett.*, 2002, **80**, 1625–1627.
27 C. H. Park and D. J. Chadi, *Phys. Rev. B: Condens. Matter Mater. Phys.*, 1998, **57**, R13961–R13964.
28 R. Das, S. Sharma and K. Mandal, *J. Magn. Magn. Mater.*, 2016, **401**, 129–137.
29 D. A. Muller, N. Nakagawa, A. Ohtomo, J. L. Grazul and H. Y. Hwang, *Nature*, 2004, **430**, 657–661.
30 M. V. Raymond and D. M. Smyth, *J. Phys. Chem. Solids*, 1996, **57**, 1507–1511.
31 X. B. Ren, *Nat. Mater.*, 2004, **3**, 91–94.
32 C. Y. Chen, Z. Y. Zhou, R. H. Liang, X. B. Zhao, W. B. Zhang and X. L. Dong, *Ceram. Int.*, 2017, **43**, 5870–5874.
33 J. Glaum, Y. A. Genenko, H. Kungl, L. A. Schmitt and T. Granzow, *J. Appl. Phys.*, 2012, **112**, 034103.
34 A. K. Nath and N. Medhi, *Bull. Mater. Sci.*, 2012, **35**, 847–852.
35 Z. Xing, Y. J. Feng and X. Y. Wei, *J. Alloys Compd.*, 2015, **627**, 238–243.
36 G. Chitgopikar, M. Chickpatil and R. L. Raibagkar, *J. Mater. Sci.: Mater. Electron.*, 2006, **17**, 963–970.
37 C. He, Z. J. Wang, X. Z. Li, X. M. Yang, X. F. Long and Z.-G. Ye, *Acta Mater.*, 2017, **125**, 498–505.
38 T. Yamashita and P. Hayes, *Appl. Surf. Sci.*, 2008, **254**, 2441–2449.
39 M. Yamaguchi, A. Ide-Ektessabi, H. Nomura and N. Yasui, *Thin Solid Films*, 2004, **447/448**, 115–118.
40 Z. G. Xia and Q. Li, *Solid State Commun.*, 2007, **142**, 323–328.
41 L. Wang, Q. Li, L. H. Xue and X. M. Liang, *J. Mater. Sci.*, 2007, **42**, 7397–7401.
42 B. Wang, X. Q. Wu, W. Ren and Z.-G. Ye, *IEEE Trans. Sonics Ultrason.*, 2015, **62**, 1016–1021.
43 I. Coondoo, N. Panwar, H. Amorin, V. E. Ramana, M. Alguero and A. Kholkin, *J. Am. Ceram. Soc.*, 2015, **98**, 3127–3135.

44 P. Pyykko, *Chem. Rev.*, 1988, **88**, 563–594.
45 K. Biswas, S. Lany and A. Zunger, *Appl. Phys. Lett.*, 2010, **96**, 201902.
46 J. P. B. Silva, M. Vorokhta, F. Dvorak, K. C. Sekhar, V. Matolin, J. Agostinho Moreira, M. Pereira and M. J. M. Gomes, *Appl. Surf. Sci.*, 2017, **400**, 453–460.
47 M. W. Zhu, H. L. Wang, H. Lei, Y. J. Zhang, N. Jia and Z. J. Wang, *Appl. Phys. A: Mater. Sci. Process.*, 2016, **122**, 364.
48 A. T. Kozakov, A. G. Kochur, L. A. Reznichenko, L. A. Shikina, A. V. Pavlenko, K. A. Googlev and V. G. Smotrakov, *J. Electron Spectrosc. Relat. Phenom.*, 2013, **186**, 14–24.
49 S. K. Das and B. K. Roul, *J. Magn. Magn. Mater.*, 2014, **363**, 77–81.
50 S. T. Zhang, G. L. Yuan, J. Wang, Y. F. Chen, G. X. Cheng and Z. G. Liu, *Solid State Commun.*, 2004, **132**, 315–318.
51 A. Hussain, N. Sinha, A. J. Joseph, K. Dhankhar, S. Goel and B. Kumar, *J. Mater. Sci.: Mater. Electron.*, 2017, **28**, 14298–14307.
52 Q. Y. Jiang, E. C. Subbarao and L. E. Cross, *J. Appl. Phys.*, 1994, **75**, 7433–7443.
53 M. Promsawat, N. Promsawat, J. W. Wong, Z. H. Luo, S. Pojprapai and S. Jiansirisomboon, *Ceram. Int.*, 2017, **43**, 13475–13482.
54 X. J. Lou, *J. Appl. Phys.*, 2009, **105**, 024101.
55 N. Kumar, T. Y. Ansell and D. P. Cann, *J. Appl. Phys.*, 2014, **115**, 154104.
56 T. Rojac, M. Kosec, B. Budic, N. Setter and D. Damjanovic, *J. Appl. Phys.*, 2010, **108**, 074107.